

Real Time Monitoring of the Dynamic Intracluster Diffusion of Single Gold Atoms into Silver Nanoclusters

Kaiyuan Zheng,[†] Victor Fung,[§] Xun Yuan,^{*,‡} De-en Jiang,[§] and Jianping Xie^{*,†,⊥}

[†]Department of Chemical and Biomolecular Engineering, National University of Singapore, 4 Engineering Drive 4, 117585 Singapore

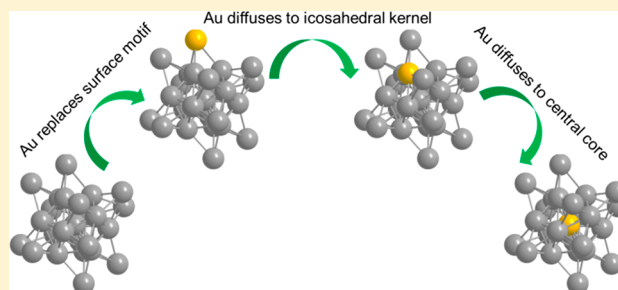
[‡]College of Materials Science and Engineering, Qingdao University of Science and Technology, Qingdao 266042, P. R. China

[§]Department of Chemistry, University of California, Riverside, California 92521, United States

[⊥]Joint School of National University of Singapore and Tianjin University, International Campus of Tianjin University, Binhai New City, Fuzhou 350207, P. R. China

Supporting Information

ABSTRACT: Alloying metal materials with heterometal atoms is an efficient way to diversify the function of materials, but in-depth understanding of the dynamic heterometallic diffusion inside the alloying materials is rather limited, especially at the atomic level. Here, we report the real-time monitoring of the dynamic diffusion process of a single gold (Au) atom into an atomically precise silver nanocluster (Ag NC), $\text{Ag}_{25}(\text{MHA})_{18}$ (MHA = 6-mercaptohexanoic acid), by using *in situ* UV–vis absorption spectroscopy in combination with mass and tandem mass spectrometry. We found that the Au heteroatom first replaces the Ag atom at the surface $\text{Ag}_2(\text{MHA})_3$ motifs of $\text{Ag}_{25}(\text{MHA})_{18}$. After that, the Au atom diffuses into the surface layer of the icosahedral Ag_{13} kernel and finally occupies the center of the alloy NCs to form the thermodynamically stable $\text{Au}@_{\text{Ag}_{24}}(\text{MHA})_{18}$ product. Density functional theory (DFT) calculations reveal that the key thermodynamic driving force is the preference of the Au heteroatom for the central site of alloy NCs. The real-time monitoring approach developed in this study could also be extended to other metal alloy systems to reveal the reaction dynamics of intracluster diffusion of heteroatoms, as well as the formation mechanisms of metal alloy nanomaterials.



INTRODUCTION

Metal alloy nanoparticles (NPs) have recently emerged as a promising class of functional materials, finding increasing acceptance in optical, catalytic, electrochemical, and biomedical applications.¹ The correlations between size, morphology, and composition of alloy NPs and their physicochemical properties have been well demonstrated; however, the doping processes of heteroatoms and their positions inside the alloy NPs are not well understood.² Moreover, the dynamic responses of alloy NPs, such as phase segregation and reconstruction or redistribution of metal atoms during chemical reactions, are presently lacking.³ These unresolved issues are mainly due to the technical limitations in characterizing the alloy atom distribution at the atomic level, especially in real-time tracking of the dynamic heteroatom movement in the alloy NPs during the reactions. Currently, real-time probing of single heteroatom behavior in the alloy NPs is challenging, although some powerful (and sometimes complicated) technologies could be employed (e.g., combination of *in situ* transmission electron spectroscopy with *in situ* extended X-ray absorption fine structure spectroscopy).⁴ Such technical challenges have constrained deep understanding of

fundamental issues of the alloy systems, such as the following questions: (i) Where are the heteroatoms inside the metal alloy NPs? (ii) Could heteroatoms replace the parental atoms or occupy vacant sites during the alloying process? (iii) Why would the heteroatoms locate at a specific position? (iv) How are the heteroatoms diffused dynamically inside the alloy NPs during the alloying process?

Ultrascale metal NPs with well-defined structures, the so-called atomically precise metal nanoclusters (NCs), may provide a good platform to address the above fundamental issues.⁵ In particular, alloying metal NCs with heteroatoms is an efficient way to produce metal alloy NCs, such as $\text{Au}_{32}\text{Ag}_{12}$, $\text{Au}_{24}\text{Pt}_1$, $\text{Au}_{24}\text{Pd}_1$, $\text{Au}_{20}\text{Ag}_1$, and $\text{Au}_{19}\text{Cd}_2$.⁶ In the final product alloy NCs, the exact positions and numbers of heteroatoms could be obtained by electrospray ionization mass spectrometry (ESI-MS) and crystallization technologies. Knowledge of the heteroatom doping mechanism is typically based on single crystal X-ray diffraction (XRD) analysis and density functional theory (DFT) simulation.⁷ However, in-depth understanding

Received: June 4, 2019

Published: October 14, 2019

of the dynamic heteroatom diffusion during the alloying process is still lacking.

Here, we report the real-time monitoring of the dynamic heteroatom diffusion into metal NCs by *in situ* UV-vis absorption spectroscopy, ESI-MS, and tandem MS (MS/MS) techniques. The key of our study is to establish a water-soluble NC alloying system, by which single Au heteroatoms could be successfully doped inside the Ag_{25} NC template to produce AuAg_{24} NC. Moreover, this alloying process is a stoichiometric reaction, and the hydrophilic metal NCs could be directly ionized, which makes real-time monitoring of the alloying process of AuAg NCs by ESI-MS possible.⁸ In addition, real-time MS/MS is applied to monitor the structural evolution of AuAg NCs during the alloying process, allowing us to observe the dynamic intracluster heteroatom diffusion during the alloying process for the first time.

RESULTS AND DISCUSSION

We used a water-soluble Ag NC, $\text{Ag}_{25}(\text{MHA})_{18}$ (MHA denotes 6-mercaptohexanoic acid), as the model parent NC for the alloying study.⁹ The solution of synthesized Ag NCs is yellowish-brown (inset of Figure 1a), and its UV-vis

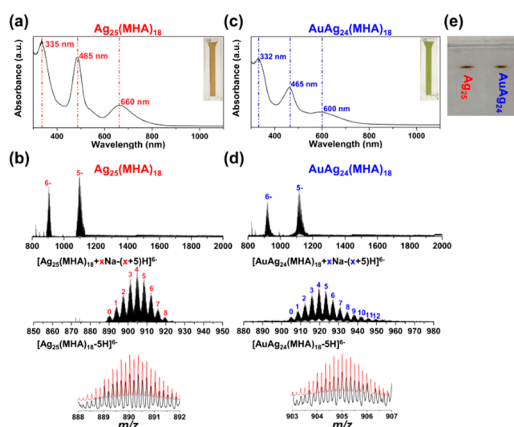


Figure 1. UV-vis absorption spectra of (a) $\text{Ag}_{25}(\text{MHA})_{18}$ and (c) $\text{AuAg}_{24}(\text{MHA})_{18}$. Insets are photographs of the NC solutions. ESI mass spectra of (b) $[\text{Ag}_{25}(\text{MHA})_{18}]^{6-}$ and (d) $[\text{AuAg}_{24}(\text{MHA})_{18}]^{6-}$. The upper panels are broad ESI mass spectra, and the charges of the ionized NC species are labeled upon each set of peaks. The middle panels are magnified ESI mass spectra of $[\text{Ag}_{25}(\text{MHA})_{18} + x\text{Na} - (x + 5)\text{H}]^{6-}$ and $[\text{AuAg}_{24}(\text{MHA})_{18} + x\text{Na} - (x + 5)\text{H}]^{6-}$. The first peak (marked as 0) represents $[\text{Ag}_{25}(\text{MHA})_{18} - 5\text{H}]^{6-}$ and $[\text{AuAg}_{24}(\text{MHA})_{18} - 5\text{H}]^{6-}$, respectively, in (b) and (d); the rest of the peaks are from the successive coordination of $[\text{Na} - \text{H}]$ of peak 0. The bottom panels are experimental (black curves) and theoretical (red curves) isotope patterns of $[\text{Ag}_{25}(\text{MHA})_{18} - 5\text{H}]^{6-}$ and $[\text{AuAg}_{24}(\text{MHA})_{18} - 5\text{H}]^{6-}$. (e) Photograph of the PAGE results of $\text{Ag}_{25}(\text{MHA})_{18}$ and $\text{AuAg}_{24}(\text{MHA})_{18}$ NCs, showing only one distinct band for each sample.

absorption spectrum displays three distinct peaks at 335, 485, and 660 nm (Figure 1a), which are the absorption characteristics of $\text{Ag}_{25}(\text{SR})_{18}$.^{9,10} In addition, the ESI-MS data further confirm the high purity of the synthesized $\text{Ag}_{25}(\text{MHA})_{18}$ (Figure 1b). Afterward, the alloying process is achieved by mixing $\text{Ag}_{25}(\text{MHA})_{18}$ with $\text{Au}(\text{I})\text{-MHA}$ complexes with the Ag_{25} -to- $\text{Au}(\text{I})$ molar ratio of 1:1 (please refer to the Supporting Information for detailed procedures). After the alloying reaction, the color of the NC solution changed to green (inset of Figure 1c), and the UV-vis absorption

spectrum of the alloy NCs shows three peaks at 332, 465, and 600 nm (Figure 1c), which are in accordance with the results reported for the $\text{AuAg}_{24}(\text{SR})_{18}$ NC.¹¹ Compared to the scant peak at 334 nm for the hydrophobic $\text{AuAg}_{24}(\text{SPhMe}_2)_{18}$ NCs (SPhMe₂ denotes 2,4-dimethylbenzenethiol),¹¹ our $\text{AuAg}_{24}(\text{MHA})_{18}$ retains the sharp peak at 332 nm from Ag_{25} NCs after alloying. The slight difference may be due to the different protection ligand and solvent environment, which maintain rather than forbid the optical transitions of NCs. In addition, ESI-MS data verify the high quality of $\text{AuAg}_{24}(\text{MHA})_{18}$ in the alloy NC solution (Figure 1d). Polyacrylamide gel electrophoresis (PAGE) analysis also shows a single band for both parent and alloy NCs (Figure 1e), providing supportive evidence for the high purity of $\text{Ag}_{25}(\text{MHA})_{18}$ and $\text{AuAg}_{24}(\text{MHA})_{18}$ in both samples.

We would like to further understand where and how the Au heteroatom locates in the AuAg_{24} alloy NCs (i.e., the alloying mechanism). It has been demonstrated that the heteroatom sitting in the core of alloy (AuAg)₂₅ NCs would greatly influence the HOMO-LUMO gap, resulting in distinct shifts of its optical features.^{6b,k,m,11} The $\text{Ag}_{25}(\text{SR})_{18}$ NC contains an icosahedral Ag_{13} core protected by six pairs of $\text{Ag}_2(\text{SR})_3$ motifs, and its HOMO-LUMO transition is mainly contributed by the atomic orbitals of the icosahedral Ag_{13} core, which also corresponds to the absorption peak at 660 nm.^{10a} Consequently, the central heteroatom doping inside the Ag_{13} core would cause a certain electronic perturbation, leading to a significant blue shift in its absorption features.^{6b,11} The synthesized $\text{AuAg}_{24}(\text{MHA})_{18}$ exhibits the same blue-shifted absorption feature (at 600 nm), so the Au heteroatom in our $\text{AuAg}_{24}(\text{MHA})_{18}$ should be located at the center of alloy NCs.^{6b,11}

To better understand the alloying mechanism of $\text{AuAg}_{24}(\text{MHA})_{18}$ from the parent $\text{Ag}_{25}(\text{MHA})_{18}$, we monitored the alloying process by *in situ* UV-vis absorption spectroscopy and ESI-MS. As shown in Figure 2a, UV-vis absorption spectra of the reaction solution indicate two stages: (i) intensity decrease of the absorption peaks from 0 to 10 min; (ii) blue shift of the absorption peaks from 10 min onward, during which the peaks at 480 and 660 nm gradually shift to 465 and 600 nm. We can also observe this transition directly from the color change of the reaction solution (insets of Figure 2a), where the solution color changed from yellowish-brown to yellowish-green and finally to green. Hence, this alloying process possibly involves two steps: diminishing of $\text{Ag}_{25}(\text{MHA})_{18}$ (0–10 min) and formation of $\text{AuAg}_{24}(\text{MHA})_{18}$ (from 10 min onward).

However, the real-time ESI-MS data provide different information on the alloying process compared to the above UV-vis absorption data. As shown in Figure 2b, $\text{AuAg}_{24}(\text{MHA})_{18}$ was formed as early as 2 min. The $[\text{Ag}_{25}(\text{MHA})_{17} - 4\text{H}]^{6-}$ and $[\text{AuAg}_{24}(\text{MHA})_{17} - 4\text{H}]^{6-}$ peaks (marked with orange and green arrows; see Figure S1 for detailed analysis) might be the reaction intermediates, which will be discussed later. After 2 min, the intensities of the $\text{Ag}_{25}(\text{MHA})_{18}$ peak sets quickly decreased, while those of the $\text{AuAg}_{24}(\text{MHA})_{18}$ peak sets increased (the relative abundance is presented in Figure 2c). Finally, $\text{Ag}_{25}(\text{MHA})_{18}$ was completely converted to $\text{AuAg}_{24}(\text{MHA})_{18}$ from 20 min onward.

Notably, the *in situ* ESI-MS data suggest that $\text{AuAg}_{24}(\text{MHA})_{18}$ is abundant at a very early reaction stage (e.g., ~60% at 5 min); however, the UV-vis absorption spectrum of the reaction solution at 10 min still shows the

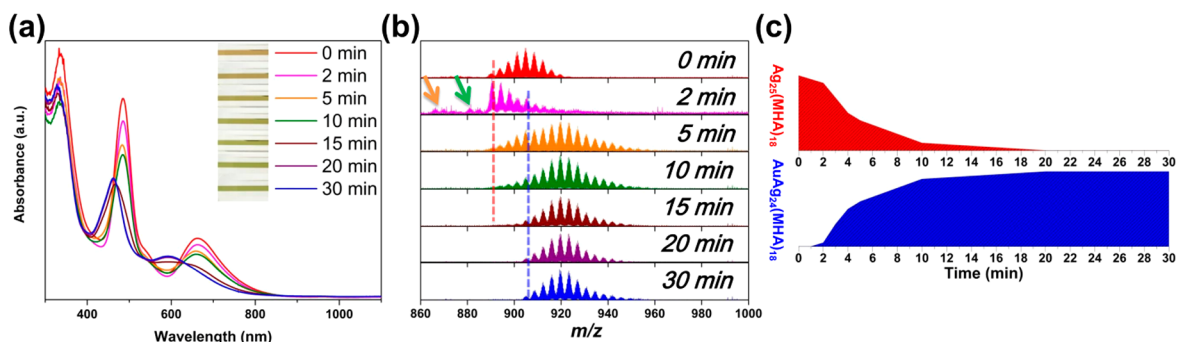


Figure 2. Time-course (a) UV-vis absorption and (b) ESI mass spectra of formation of $\text{AuAg}_{24}(\text{MHA})_{18}$ from $\text{Ag}_{25}(\text{MHA})_{18}$. Insets are photographs of the reaction solution at different time points. The dashed red line marks the peak of $[\text{Ag}_{25}(\text{MHA})_{18} - 5\text{H}]^{6-}$, and the dashed blue line marks the peak of $[\text{AuAg}_{24}(\text{MHA})_{18} - 5\text{H}]^{6-}$. The orange arrow marks the peak of $[\text{Ag}_{25}(\text{MHA})_{17} - 4\text{H}]^{6-}$, and the green arrow marks the peak of $[\text{AuAg}_{24}(\text{MHA})_{17} - 4\text{H}]^{6-}$. (c) Time-dependent abundance of $\text{Ag}_{25}(\text{MHA})_{18}$ and $\text{AuAg}_{24}(\text{MHA})_{18}$.

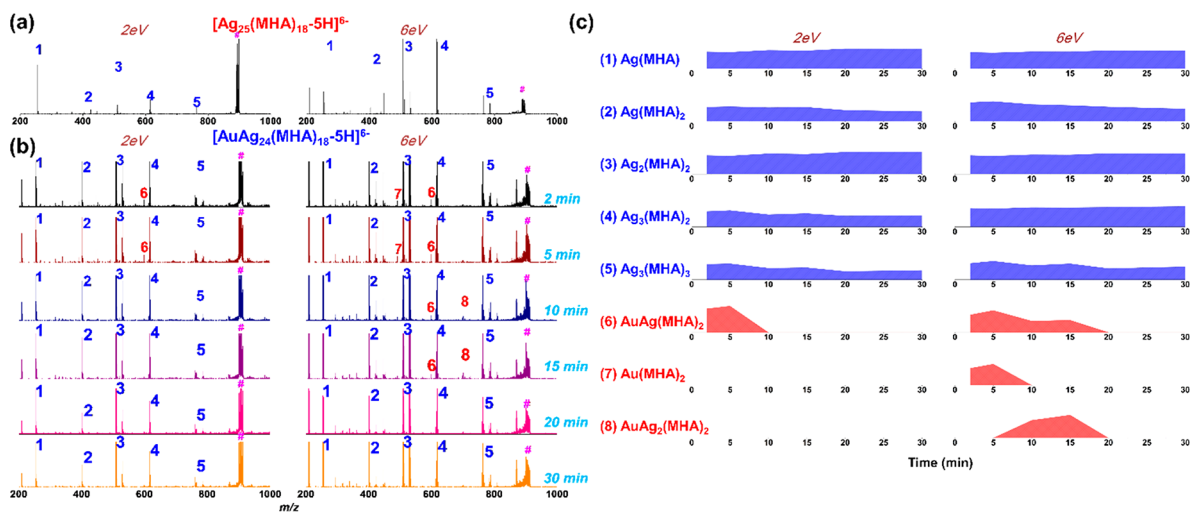


Figure 3. (a) Tandem mass spectra of $[\text{Ag}_{25}(\text{MHA})_{18} - 5\text{H}]^{6-}$ (centered at $m/z = 890$) obtained at collision energies of 2 and 6 eV. (b) Time-course tandem mass spectra of $[\text{AuAg}_{24}(\text{MHA})_{18} - 5\text{H}]^{6-}$ (centered at $m/z = 905$) obtained at collision energies of 2 and 6 eV. (c) Time-dependent abundance of each fragment. The number in front of each molecular formula corresponds to the labeled number of each fragment in (a) and (b).

characteristic absorption of $\text{Ag}_{25}(\text{MHA})_{18}$ without a blue shift. As mentioned above, only the center-doped $\text{Au@Ag}_{24}(\text{MHA})_{18}$ exhibits a significant blue-shifted optical absorption feature; therefore, we could deduce that the Au heteroatom is not at the central position in the early reaction stage and is instead sitting at the surface motif of alloy NCs, as the surface motif would not contribute significantly to the HOMO-LUMO transition.^{6b,11} Afterward, the Au heteroatom may gradually diffuse into the central position due to the structural symmetry and thermodynamic stability requirements, as proven by UV-vis absorption spectra transition during the second stage (the blue-shift process) after 10 min. It is worth noting that UV-vis absorption spectra of the samples during the conversion are all crossed at one point during this blue-shift transition process, which indicates that the reaction is a single molecular reaction, further supporting that the diffusion of the Au heteroatom is an intracuster reaction rather than an intercluster reaction. In addition, similar to some organic reactions, this Au heteroatom alloying reaction also follows a stoichiometric reaction process (Figures S2 and S3).

To verify our assumption that the Au heteroatom has dynamically diffused from the surface $\text{Ag}_2(\text{MHA})_3$ motif into the center of the icosahedral Ag_{13} core, we used MS/MS to

monitor the fragmentation patterns of $\text{AuAg}_{24}(\text{MHA})_{18}$ in real time. MS/MS is a powerful tool to deduce molecular structure through fragmentation patterns and could also provide useful information regarding the structures of molecular-like metal NCs.^{6f,12} In general, the pristine ions with the desired m/z are selected in the first MS analysis (MS-1) and then subjected to a successive MS examination (MS-2), where the fragmentation spectra of the pristine ions could be recorded under varied collision energies. In addition, our water-soluble NCs could be easily (and directly) ionized, which makes possible the direct MS/MS measurement without additional post-treatment. Therefore, we could acquire the real-time structural information on NCs during the alloying process by tracking the position of the Au heteroatom.

First, pure $\text{Ag}_{25}(\text{MHA})_{18}$ is used as a reference (see details in the Supporting Information). As shown in Figure 3a, five fragments could be observed at a low collision energy (2 eV), and their molecular formulas are shown in Figure 3c (detailed analysis in Figures S4–S8). The three major fragments are as follows: (1) $[\text{Ag}(\text{MHA}) - \text{H}]^-$, (2) $[\text{Ag}(\text{MHA})_2]^-$, and (3) $[\text{Ag}_2(\text{MHA})_2 - \text{H}]^-$, which could be generated from the surface $\text{Ag}_2(\text{MHA})_3$ motifs. At a higher collision energy of 6 eV, the intensities of fragments (4) $[\text{Ag}_3(\text{MHA})_2 - 2\text{H}]^-$ and

(5) $[\text{Ag}_3(\text{MHA})_3 - \text{H}]^-$ greatly increase. According to the crystal structure of Ag_{25} , the third Ag atom in fragments (4) and (5) could be from the icosahedral Ag_{13} kernel, since one surface motif only contains two Ag atoms. Therefore, we could use the low and high collision energy modes to obtain the information on surface motif exfoliation and inner icosahedral kernel exfoliation, respectively.

Two such collision energy modes (2 and 6 eV) are thus applied to $\text{AuAg}_{24}(\text{MHA})_{18}$ to monitor the fragmentation behavior at different times (Figure 3b,c). At 2 and 5 min, one more fragment, (6) $[\text{AuAg}(\text{MHA})_2 - \text{H}]^-$ (similar to $[\text{Ag}_2(\text{MHA})_2 - \text{H}]^-$, Figure S9), is observed at both low and high collision energies, indicating the location of Au heteroatom at the surface motifs. Fragment (7) $[\text{Au}(\text{MHA})_2 - \text{H}]^-$ (Figure S10) is not observed at low collision energy but appears at the high collision energy and might be derived from the second fragmentation of $[\text{AuAg}(\text{MHA})_2 - \text{H}]^-$ after higher energy collision. Moreover, we analyzed the intermediate $[\text{AuAg}_{24}(\text{MHA})_{17} - 4\text{H}]^{6-}$ at 2 min (Figure S11), and fragment (7) also appears, further indicating that the Au heteroatom is located at the surface motifs. Taken together, the Au heteroatom is confirmed to locate at the surface motifs of alloy NCs in the early alloying stage.

In stark contrast, the Au-containing fragments could not be observed at the low collision energy after 10 min, suggesting that the Au heteroatom is no longer at the surface motifs of the alloy NCs. However, when we applied the high collision energy, a new fragment (8) $[\text{AuAg}_2(\text{MHA})_2 - 2\text{H}]^-$ (similar to $[\text{Ag}_3(\text{MHA})_2 - 2\text{H}]^-$, Figure S12) emerges, indicating that the Au heteroatom has diffused into the icosahedral kernel. This Au atom could only be from the icosahedral kernel, rather than the surface motifs of alloy NCs; otherwise, the Au-containing fragments could be observed at the low collision energy. Furthermore, a very weak fragment (6) also appears at the high collision energy instead of the low energy collision, which may be derived from the second fragmentation of $[\text{AuAg}_2(\text{MHA})_2 - 2\text{H}]^-$.

From 20 min onward, no more Au-containing fragments could be observed at either low or high collision energies. The fragmentation patterns are the same as those of $\text{Ag}_{25}(\text{MHA})_{18}$, indicating that the Au heteroatom has diffused into the central core of alloy NCs. This is also evidenced by the real-time UV-vis absorption spectra (Figure 2a), where the reaction solution only exhibits characteristic absorption of the center-doped AuAg_{24} NC from 20 min onward. In addition, we used X-ray photoelectron spectroscopy (XPS) to measure the time-dependent oxidation states of the Au of $\text{AuAg}_{24}(\text{MHA})_{18}$ (Figure S13). The Au is primarily Au^{I} ($\text{Au } 4f_{7/2} \sim 85 \text{ eV}$) during the early reaction stage, then becomes a mixture of Au^{I} and Au^0 ($\text{Au } 4f_{7/2} \sim 84.5 \text{ eV}$), and finally changes to Au^0 ($\text{Au } 4f_{7/2} \sim 84 \text{ eV}$). These data correspond well with the oxidation states of Au at the surface motifs (Au^{I}), as well as at the surface layer of the icosahedral kernel and in the central core (Au^0) of alloy NCs, further verifying the Au heteroatom diffusion from the surface to the core of $\text{AuAg}_{24}(\text{MHA})_{18}$.

Tandem MS is an efficient technology to exfoliate metal NCs from the surface motifs to the inner core by varying the collision energies,^{6f,12c} thus providing useful fragmentation information to probe the structural evolution of metal NCs. To further prove the capability of tandem MS in this respect, we chose $\text{Au}_2\text{Ag}_{23}(\text{MHA})_{18}$ as a reference for tandem MS analysis under two collision energies (2 and 6 eV). As shown in Figure S14, fragments (6) $[\text{AuAg}(\text{MHA})_2 - \text{H}]^-$ and (7) $[\text{Au}$

$(\text{MHA})_2 - \text{H}]^-$ were detected throughout the entire reaction from the beginning, which suggests that a Au atom is always located at the surface motifs of alloy NCs without diffusing inside. Interestingly, fragment (8) $[\text{AuAg}_2(\text{MHA})_2 - 2\text{H}]^-$ only appeared from 10 to 20 min under high collision energy (similar to the fragmentation behavior of $\text{AuAg}_{24}(\text{MHA})_{18}$), which indicates the internalization movement of the heteroatom Au during the alloying process. For the Au atom distribution in $\text{Au}_2\text{Ag}_{23}(\text{MHA})_{18}$, one Au atom would be on the surface motif, while the other Au atom would move into the central position. This result matches well with the UV-vis absorption features of $\text{Au}_2\text{Ag}_{23}(\text{MHA})_{18}$ (Figure S3), suggesting that the second Au atom is at the surface motif of the alloy NCs instead of inside the icosahedral Ag_{13} core. The successful analysis of the second heteroatom Au position in $\text{Au}_2\text{Ag}_{23}(\text{MHA})_{18}$ further proves that real-time tandem MS is a powerful tool for probing the structural evolution of metal alloy NCs.

It is interesting to note that when we used different ligand-produced $\text{Au}(\text{I})\text{-SR}$ complexes to react with $\text{Ag}_{25}(\text{MHA})_{18}$, the final products were all $\text{AuAg}_{24}(\text{MHA})_{18}$ without any ligand hybridization (Figure S15). This might be explained by the symmetric consideration, as only the most thermodynamically favorable NCs with the highest symmetry (e.g., the 18 ligands are all the same) could be formed. Furthermore, we used ESI-MS to monitor the alloying process of $\text{Ag}_{25}(\text{MHA})_{18}$ with $\text{Au}(\text{I})\text{-GSH}$ (GSH denotes L-glutathione reduced; Figure S16) and found that GSH never doped inside the alloy NCs (Figure S16b). Interestingly, when we magnified the low m/z regions of ESI-MS spectra, the $[\text{Ag}(\text{SG}) - \text{H}]^-$ species was observed from the very beginning of the reaction (Figure S16c), which implies that the GSH combined with the replaced Ag atom dissociated from the surface motifs of Ag NCs and subsequently departed from the final alloy NCs. However, if Pt, Pd, Cu, Hg, or Cd were used as a heteroatom source, no alloy NCs could be formed (Figure S17). This is different from the Au NCs-based alloying system and the hydrophobic NCs system, and future experimental and theoretical studies are needed to clarify this difference.

From the above experimental evidence, we proposed the intracuster Au heteroatom diffusion mechanism in the alloying process of AuAg NCs, as illustrated in Figure 4. First, the Au

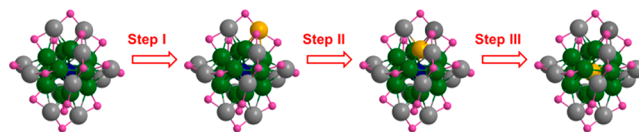


Figure 4. Proposed intracuster Au heteroatom diffusion mechanism. Color scheme: Ag atoms on the surface staple motifs (gray); Ag atoms on the surface layer of the icosahedral kernel (green); central Ag atom of the icosahedral core (blue); gold atom (yellow); sulfur atoms of the MHA ligand on the surface staple motifs (pink).

heteroatom exchanges with one Ag atom on the surface $\text{Ag}_2(\text{MHA})_3$ motif of Ag_{25} to form $\text{Ag}@\text{Ag}_{12}@\text{AuAg}_{11}(\text{MHA})_{18}$ (step I). As the as-formed $\text{Ag}@\text{Ag}_{12}@\text{AuAg}_{11}(\text{MHA})_{18}$ is not the thermodynamically favorable product, the Au heteroatom would further diffuse from the surface motif to the surface layer of the icosahedral Ag_{13} kernel to generate $\text{Ag}@\text{AuAg}_{11}@\text{Ag}_{12}(\text{MHA})_{18}$ (step II). In this step, a galvanic reaction is presumed to occur, and the $\text{Au}(\text{I})$ could be reduced to $\text{Au}(0)$. Finally, the Au heteroatom would diffuse

into the center of alloy NCs to form $\text{Au}@Ag_{12}@Ag_{12}(\text{MHA})_{18}$, with the best structural symmetry and the highest thermodynamic stability (step III). This experimental observation differs from the previous speculation that Au(I) could directly approach the center of Ag_{25} NC and exchange the central Ag atom *via* galvanic reaction (e.g., Au^{I} is reduced to Au^{0} by the central Ag^{0} atom).¹¹

To corroborate the proposed mechanism in Figure 4, we have employed DFT to compute the thermodynamic driving force of the displacement of Ag atom by Au atom, as well as the diffusion of the Au atom into the cluster center. As shown in Table 1, the overall reaction is indeed favorable ($\Delta E =$

Table 1. Computed Reaction Energetics for the Proposed Mechanism

step	reaction	$\Delta E(\text{eV})$
step I	$Ag_{25}(\text{MHA})_{18}^{-} + Au(\text{MHA})_2^{-} \rightarrow Ag@Ag_{12}@AuAg_{11}(\text{MHA})_{18}^{-} + Ag(\text{MHA})_2^{-}$	0.06
step II	$Ag@Ag_{12}@AuAg_{11}(\text{MHA})_{18}^{-} \rightarrow Ag@AuAg_{11}@Ag_{12}(\text{MHA})_{18}^{-}$	0.10
step III	$Ag@AuAg_{11}@Ag_{12}(\text{MHA})_{18}^{-} \rightarrow Au@Ag_{12}@Ag_{12}(\text{MHA})_{18}^{-}$	-0.31
overall	$Ag_{25}(\text{MHA})_{18}^{-} + Au(\text{MHA})_2^{-} \rightarrow Au@Ag_{12}@Ag_{12}(\text{MHA})_{18}^{-} + Ag(\text{MHA})_2^{-}$	-0.15

-0.15 eV). More interestingly, the computed energetics of step I ($\Delta E_1 = 0.06$ eV), step II ($\Delta E_2 = 0.10$ eV), and step III ($\Delta E_3 = -0.31$ eV) suggest that the first two steps are almost thermoneutral, and the overall reaction is mainly driven by the strong preference of the Au heteroatom for the center of alloy NCs (step III). We further explored the detailed reaction pathway through energy profiling (Figure S18) and found that the presence of an adsorbed $Ag(\text{SR})_2$ could significantly lower the barriers of a concerted mechanism. First, $Au(\text{SR})_2$ can adsorb onto $Ag_{25}(\text{SR})_{18}$ with an adsorption energy of -0.41 eV to form a planar AuS_4 species (Figure S18, B). A facile rearrangement of the two SR groups can then lower the energy to -0.56 eV (Figure S18, C). The Au can subsequently insert into the staple dimer (Figure S18, D) and displace a Ag in a concerted mechanism, with a barrier of 0.81 eV. This matches well with the simultaneous appearance of two reaction intermediates, $Ag_{25}(\text{MHA})_{17}$ and $AuAg_{24}(\text{MHA})_{17}$, during the early reaction stage (Figure 2b).¹³ After that, while the $Ag(\text{SR})_2$ species is still adsorbed onto the $AuAg_{24}(\text{SR})_{18}$, the Au can exchange through the shell in another concerted three-atom triangular-rotation mechanism involving the Au, the Ag from $Ag(\text{SR})_2$, and a Ag atom from the icosahedral shell (Figure S18, F; see also the uploaded movie file of Supporting Information). This mechanism has a barrier of 1.04 eV, which is significantly lowered by the presence of the adsorbed $Ag(\text{SR})_2$. Without the $Ag(\text{SR})_2$, the barriers are found to be over 2 eV. Finally, the Au can exchange with the central core Ag in a thermodynamically favored process, as discussed before (Figure S18, H). During the DFT simulation, we applied relative energies to the NCs with the same size and very close compositions instead of the DFT-GGA-calculated energy, which is more reliable, and the uncertainty is on the order of 0.1 eV due to the error cancellation. It is reasonable to assume that the NCs will have very similar solvation energies that would be canceled out. Therefore, the relative energies that we obtained, though small (0.1–0.3 eV in magnitude), do show relative stability consistent with the experimental observations.

This driving force of Au heteroatom diffusion into the center of the Ag_{25} may originate from the structural difference between Ag_{25} and $AuAg_{24}$. According to the reported crystal structure, all 12 Ag atoms on the surface motif of $AuAg_{24}$ occupy the centers of 12 triangular faces of the icosahedral $AuAg_{12}$ kernel, while 3 Ag atoms on the surface motif of Ag_{25} stay away from the triangular faces.^{10a,11} As a result, the distortion of motifs of Ag_{25} is relieved after Au doping into the central core of $AuAg_{24}$, and the bond lengths of $Ag_{\text{icosahedron}}-S$ and $Ag_{\text{motif}}-S$ in $AuAg_{24}$ are found to be slightly shorter than those in Ag_{25} .¹¹ This is also supported by the improved stability of $AuAg_{24}$ as opposed to Ag_{25} (Figure S19). All of these data suggest that the $AuAg_{24}$ NCs would be the most thermodynamically stable product if the Au heteroatom locates at the central core of the NCs; therefore, the incorporated Au atom would diffuse from the surface motif to the center of NCs to reach the most stable state.

CONCLUSION

In summary, we have reported the real-time monitoring of the dynamic intracuster Au heteroatom diffusion by using *in situ* UV-vis absorption spectrometry, as well as ESI mass and tandem mass spectrometry, leveraging the easy and direct ionization of water-soluble NCs in the reaction solution. The Au heteroatom first exchanges with the Ag atom on the surface $Ag_2(\text{MHA})_3$ motif of Ag_{25} to form $Ag@Ag_{12}@AuAg_{11}(\text{MHA})_{18}$, then diffuses to the surface layer of the icosahedral Ag_{13} kernel through galvanic reaction to generate $Ag@AuAg_{11}@Ag_{12}(\text{MHA})_{18}$, and finally moves into the center of alloy NCs to produce the $Au@Ag_{12}@Ag_{12}(\text{MHA})_{18}$. DFT calculations of the energetics show that the key thermodynamic driving force is the preference of Au heteroatom for the center of alloy NCs. This study reveals the dynamic heteroatom diffusion process inside metal alloy NCs at the atomic level, which would boost the development of novel alloy materials for both fundamental and applied fields.

EXPERIMENTAL SECTION

Materials. Ultrapure water (18.2 M Ω) was used throughout the study. All glassware and magnetic stir bars were washed with *aqua regia*, rinsed with abundant ethanol and ultrapure water, and dried in an oven before use. All chemicals are commercially available; they were used as received: gold(III) chloride trihydrate ($\text{HAuCl}_4 \cdot 3\text{H}_2\text{O}$), 2-mercaptoethanol (MetH), 3-mercaptopropionic acid (MPA), 4-mercaptopbutyric acid (MBA), 6-mercaptophexanoic acid (MHA), sodium borohydride (NaBH_4), and L-glutathione reduced (GSH) were purchased from Sigma-Aldrich; silver nitrate (AgNO_3) and sodium hydroxide (NaOH) were purchased from Merck.

Instruments. UV-vis absorption spectra of metal nanoclusters (NCs) were recorded on a Shimadzu UV-1800 photospectrometer. Electrospray ionization mass spectra (ESI-MS) and tandem MS were acquired on a Bruker microTOF-Q system. Inductively coupled plasma optical emission spectrometry (ICP-OES) was used to determine the concentration of metal atoms in solution, which was measured through iCAP 6000 Series (Thermo Scientific). Native polyacrylamide gel electrophoresis (PAGE) was conducted on a Bio-Rad Mini-Protean Tetra Cell system. The stacking and resolving gels contained 4 and 20 wt % acrylamide monomers, respectively. The electrophoresis was allowed to run at 4 °C with a constant voltage of 150 V for 80 min. X-ray photoelectron spectroscopy (XPS) was conducted on a Kratos AXIS Ultra^{DL} spectrometer, and samples of the reaction solution were quickly frozen at -80 °C at different time points to measure the corresponding oxidation states of the Au element.

Synthesis of Ag₂₅(MHA)₁₈ NCs. The synthesis of Ag₂₅ NCs was conducted at 50 °C. Freshly prepared aqueous solutions of AgNO₃ (20 mM, 0.125 mL) and MHA (10 mM, 0.75 mL) were mixed in water (4.025 mL), leading to the formation of white Ag(I)–MHA complexes. Afterward, 0.1 mL of a freshly prepared NaBH₄ solution (produced by dissolving 43 mg of NaBH₄ powder into 10 mL of 0.2 M NaOH solution) was added to the solution under stirring condition. The Ag₂₅(MHA)₁₈ NCs were collected after 30 min. After that, the synthesized Ag₂₅(MHA)₁₈ NCs were purified by running the samples through PD-10 desalting columns (GE Healthcare UK Ltd.) containing 8.3 mL of Sephadex™ G-25 medium with a molecular weight exclusion limit of 5000 Da, and with an elution buffer of 10 mM NaOH solution. Finally, the concentration of Ag species in Ag₂₅ NC solution was analyzed by ICP-OES.

Synthesis of AuAg₂₄(MHA)₁₈ NCs. The Au(I)–MHA complexes were prepared as follows: an aqueous solution of HAuCl₄ (40 mM, 0.1 mL) was mixed with a freshly prepared MHA solution (10 mM, 0.8 mL), and then a 0.1 M NaOH solution was added to adjust the pH to 11. Other ligand-protected Au(I) complexes were prepared by using the same strategy, except for the replacement of ligand solutions. In a typical synthesis of AuAg₂₄(MHA)₁₈ NCs, the Au(I)–MHA complexes were added into the purified Ag₂₅ NC solution under stirring condition with a molar ratio of Au atoms to Ag atoms of 1:25 (i.e., the molar ratio of the Au atoms in Au(I)–MHA complexes to Ag₂₅ NCs is 1:1). Afterward, the solution was quickly shaken on a vortex device to ensure sufficient mixing, and the reaction solution was used for *in situ* measurement. The final AuAg₂₄ NC product was collected after 30 min.

Real-Time Monitoring of the Transition from Ag₂₅(MHA)₁₈ to AuAg₂₄(MHA)₁₈ by ESI-MS/MS. For Ag₂₅(MHA)₁₈NCs, the [Ag₂₅(MHA)₁₈ – SH]^{6–} species (at *m/z* = 890 in the ESI mass spectra) was selected as the model ion, and the low collision energy (2 eV) and high collision energy (6 eV) of ESI-MS/MS were separately applied to this selected species to obtain the fragmentation patterns. For AuAg₂₄(MHA)₁₈NCs, the [AuAg₂₄(MHA)₁₈ – SH]^{6–} species (at *m/z* = 905 in the ESI mass spectra) was chosen as the model ion, and the low collision energy (2 eV) and high collision energy (6 eV) of ESI-MS/MS were separately applied to this selected species to obtain the fragmentation patterns. The ESI-MS/MS data were collected in real time for further analysis.

Computational Method. The density functional theory (DFT) calculations were performed using the TPSS form¹⁴ of the meta-GGA (generalized gradient approximation)¹⁵ functional for the electron exchange and correlation, as implemented the quantum chemistry program Turbomole V6.5.¹⁶ Def2-SV(P) basis sets were used for the main group elements,¹⁷ and effective core potentials with 19 valence electrons were used for Au, including scalar relativistic corrections.¹⁸ The kinetic pathway studies were performed using the Vienna *ab initio* Simulation Package (VASP).¹⁹ The Perdew–Burke–Ernzerhof (PBE)¹⁵ functional form of the generalized-gradient approximation (GGA) for electron exchange and correlation energies were used in the calculations. All calculations were performed with spin polarization. The projector-augmented wave method (PAW) was used to describe the electron–core interaction,^{19a,20} with a kinetic energy cutoff of 450 eV for the surface calculations. The transition states (TS) were obtained using the nudged elastic band (NEB)²¹ method with a force convergence criterion of 0.05 eV/Å.

■ ASSOCIATED CONTENT

Supporting Information

The Supporting Information is available free of charge on the ACS Publications website at DOI: 10.1021/jacs.9b05776.

Figures of ESI mass spectra, UV–vis absorption, isotope analysis of the fragments, tandem mass spectra, XPS spectra, and energy profiles and transition state structures (PDF)

Movie of the reaction process (AVI)

■ AUTHOR INFORMATION

Corresponding Authors

*yuanxun@qust.edu.cn

*chexiej@nus.edu.sg

ORCID

Kaiyuan Zheng: 0000-0003-1876-7712

De-en Jiang: 0000-0001-5167-0731

Jianping Xie: 0000-0002-3254-5799

Notes

The authors declare no competing financial interest.

■ ACKNOWLEDGMENTS

We acknowledge the financial support from the Ministry of Education, Singapore, Academic Research Grant R-279-000-538-114, Taishan Scholar Foundation (tsqn201812074, China), and the Young Talents Joint Fund of Shandong Province (ZR2019YQ07, China). DFT computation (V.F. and D.J.) was sponsored by the U.S. Department of Energy, Office of Science, Office of Basic Energy Sciences, Chemical Sciences, Geosciences, and Biosciences Division.

■ REFERENCES

- (1) (a) Ferrando, R.; Jellinek, J.; Johnston, R. L. Nanoalloys: from theory to applications of alloy clusters and nanoparticles. *Chem. Rev.* **2008**, *108*, 845. (b) Gilroy, K. D.; Ruditskiy, A.; Peng, H.-C.; Qin, D.; Xia, Y. Bimetallic nanocrystals: syntheses, properties, and applications. *Chem. Rev.* **2016**, *116*, 10414. (c) Cortie, M. B.; McDonagh, A. M. Synthesis and optical properties of hybrid and alloy plasmonic nanoparticles. *Chem. Rev.* **2011**, *111*, 3713. (d) Liu, H.-L.; Nosheen, F.; Wang, X. Noble metal alloy complex nanostructures: controllable synthesis and their electrochemical property. *Chem. Soc. Rev.* **2015**, *44*, 3056. (e) You, H.; Yang, S.; Ding, B.; Yang, H. Synthesis of colloidal metal and metal alloy nanoparticles for electrochemical energy applications. *Chem. Soc. Rev.* **2013**, *42*, 2880. (f) Wang, D.; Li, Y. Bimetallic nanocrystals: liquidphase synthesis and catalytic applications. *Adv. Mater.* **2011**, *23*, 1044. (g) Chen, P.-C.; Liu, M.; Du, J. S.; Meckes, B.; Wang, S.; Lin, H.; Dravid, V. P.; Wolverton, C.; Mirkin, C. A. Interface and heterostructure design in polyelemental nanoparticles. *Science* **2019**, *363*, 959. (h) Lim, B.; Jiang, M.; Camargo, P. H.; Cho, E. C.; Tao, J.; Lu, X.; Zhu, Y.; Xia, Y. Pd–Pt bimetallic nanodendrites with high activity for oxygen reduction. *Science* **2009**, *324*, 1302. (i) Kluender, E. J.; Hedrick, J. L.; Brown, K. A.; Rao, R.; Meckes, B.; Du, J. S.; Moreau, L. M.; Maruyama, B.; Mirkin, C. A. Catalyst discovery through megalibraries of nanomaterials. *Proc. Natl. Acad. Sci. U. S. A.* **2019**, *116*, 40. (j) Chen, P.-C.; Liu, G.; Zhou, Y.; Brown, K. A.; Chernyak, N.; Hedrick, J. L.; He, S.; Xie, Z.; Lin, Q.-Y.; Dravid, V. P.; O'Neill-Slawecki, S. A.; Mirkin, C. A. Tip-directed synthesis of multimetallic nanoparticles. *J. Am. Chem. Soc.* **2015**, *137*, 9167.
- (2) (a) Hwang, B.-J.; Sarma, L. S.; Chen, J.-M.; Chen, C.-H.; Shih, S.-C.; Wang, G.-R.; Liu, D.-G.; Lee, J.-F.; Tang, M.-T. Structural models and atomic distribution of bimetallic nanoparticles as investigated by X-ray absorption spectroscopy. *J. Am. Chem. Soc.* **2005**, *127*, 11140. (b) Ding, Y.; Fan, F.; Tian, Z.; Wang, Z. L. Atomic structure of Au–Pd bimetallic alloyed nanoparticles. *J. Am. Chem. Soc.* **2010**, *132*, 12480. (c) Hong, J. W.; Kim, D.; Lee, Y. W.; Kim, M.; Kang, S. W.; Han, S. W. Atomic-distribution-dependent electrocatalytic activity of Au–Pd bimetallic nanocrystals. *Angew. Chem., Int. Ed.* **2011**, *50*, 8876.
- (3) (a) Zucig, B.; Wang, L.; Heine, C.; Zakharov, D. N.; Lechner, B. A.; Stach, E. A.; Biener, J.; Salmeron, M.; Madix, R. J.; Friend, C. M. Dynamic restructuring drives catalytic activity on nanoporous gold–silver alloy catalysts. *Nat. Mater.* **2017**, *16*, 558. (b) Cui, C.; Gan, L.; Heggen, M.; Rudi, S.; Strasser, P. Compositional segregation in shaped Pt alloy nanoparticles and their structural behaviour during electrocatalysis. *Nat. Mater.* **2013**, *12*, 765. (c) Niu, Z.; Becknell, N.;

- Yu, Y.; Kim, D.; Chen, C.; Kornienko, N.; Somorjai, G. A.; Yang, P. Anisotropic phase segregation and migration of Pt in nanocrystals en route to nanoframe catalysts. *Nat. Mater.* **2016**, *15*, 1188. (d) Tao, F.; Grass, M. E.; Zhang, Y.; Butcher, D. R.; Renzas, J. R.; Liu, Z.; Chung, J. Y.; Mun, B. S.; Salmeron, M.; Somorjai, G. A. Reaction-driven restructuring of Rh-Pd and Pt-Pd core-shell nanoparticles. *Science* **2008**, *322*, 932. (e) Chi, M.; Wang, C.; Lei, Y.; Wang, G.; Li, D.; More, K. L.; Lupini, A.; Allard, L. F.; Markovic, N. M.; Stamenkovic, V. R. Surface faceting and elemental diffusion behaviour at atomic scale for alloy nanoparticles during in situ annealing. *Nat. Commun.* **2015**, *6*, 8925.
- (4) (a) van der Hoeven, J. E.; Welling, T. A.; Silva, T. A.; van den Reijen, J. E.; La Fontaine, C.; Carrier, X.; Louis, C.; van Blaaderen, A.; de Jongh, P. E. In situ observation of atomic redistribution in alloying gold-silver nanorods. *ACS Nano* **2018**, *12*, 8467. (b) Yamada, T.; Kojima, T.; Abe, E.; Kameoka, S.; Murakami, Y.; Gille, P.; Tsai, A. P. Probing single Pt atoms in complex intermetallic $\text{Al}_{13}\text{Fe}_4$. *J. Am. Chem. Soc.* **2018**, *140*, 3838.
- (5) (a) Jin, R.; Zeng, C.; Zhou, M.; Chen, Y. Atomically precise colloidal metal nanoclusters and nanoparticles: fundamentals and opportunities. *Chem. Rev.* **2016**, *116*, 10346. (b) Yao, Q.; Yuan, X.; Chen, T.; Leong, D. T.; Xie, J. Engineering functional metal materials at the atomic level. *Adv. Mater.* **2018**, *30*, 1802751. (c) Yao, Q.; Chen, T.; Yuan, X.; Xie, J. Toward total synthesis of thiolate-protected metal nanoclusters. *Acc. Chem. Res.* **2018**, *51*, 1338. (d) Chakraborty, I.; Pradeep, T. Atomically precise clusters of noble metals: emerging link between atoms and nanoparticles. *Chem. Rev.* **2017**, *117*, 8208. (e) Wu, Z.; Yao, Q.; Zang, S.; Xie, J. Directed self-assembly of ultrasmall metal nanoclusters. *ACS Mater. Lett.* **2019**, *1*, 237.
- (6) (a) Wang, S.; Li, Q.; Kang, X.; Zhu, M. Customizing the structure, composition, and properties of alloy nanoclusters by metal exchange. *Acc. Chem. Res.* **2018**, *51*, 2784. (b) Liu, Y.; Chai, X.; Cai, X.; Chen, M.; Jin, R.; Ding, W.; Zhu, Y. Central doping of a foreign atom into the silver cluster for catalytic conversion of CO_2 toward C-C bond formation. *Angew. Chem., Int. Ed.* **2018**, *57*, 9775. (c) Qian, H.; Jiang, D.-e.; Li, G.; Gayathri, C.; Das, A.; Gil, R. R.; Jin, R. Monoplatinum doping of gold nanoclusters and catalytic application. *J. Am. Chem. Soc.* **2012**, *134*, 16159. (d) Soldan, G.; Aljuhani, M. A.; Bootharaju, M. S.; AbdulHalim, L. G.; Parida, M. R.; Emwas, A. H.; Mohammed, O. F.; Bakr, O. M. Gold doping of silver nanoclusters: A 26-fold enhancement in the luminescence quantum yield. *Angew. Chem., Int. Ed.* **2016**, *55*, 5749. (e) Barrabés, N.; Zhang, B.; Bürgi, T. Racemization of chiral $\text{Pd}_2\text{Au}_{36}(\text{SC}_2\text{H}_4\text{Ph})_{24}$: Doping increases the flexibility of the cluster surface. *J. Am. Chem. Soc.* **2014**, *136*, 14361. (f) Yao, Q.; Feng, Y.; Fung, V.; Yu, Y.; Jiang, D.-e.; Yang, J.; Xie, J. Precise control of alloying sites of bimetallic nanoclusters via surface motif exchange reaction. *Nat. Commun.* **2017**, *8*, 1555. (g) Li, Y.; Luo, T.-Y.; Zhou, M.; Song, Y.; Rosi, N. L.; Jin, R. A correlated series of Au/Ag nanoclusters revealing the evolutionary patterns of asymmetric Ag doping. *J. Am. Chem. Soc.* **2018**, *140*, 14235. (h) Li, Q.; Lambright, K. J.; Taylor, M. G.; Kirschbaum, K.; Luo, T.-Y.; Zhao, J.; Mpourmpakis, G.; Mokashi-Punekar, S.; Rosi, N. L.; Jin, R. Reconstructing the surface of gold nanoclusters by cadmium doping. *J. Am. Chem. Soc.* **2017**, *139*, 17779. (i) Zhu, M.; Wang, P.; Yan, N.; Chai, X.; He, L.; Zhao, Y.; Xia, N.; Yao, C.; Li, J.; Deng, H.; Zhu, Y.; Yong, P.; Wu, Z. The fourth alloying mode by way of anti-galvanic reaction. *Angew. Chem., Int. Ed.* **2018**, *57*, 4500. (j) Yang, H.; Wang, Y.; Huang, H.; Gell, L.; Lehtovaara, L.; Malola, S.; Häkkinen, H.; Zheng, N. All-thiol-stabilized Ag_{44} and $\text{Au}_{12}\text{Ag}_{32}$ nanoparticles with single-crystal structures. *Nat. Commun.* **2013**, *4*, 2422. (k) Wang, S.; Song, Y.; Jin, S.; Liu, X.; Zhang, J.; Pei, Y.; Meng, X.; Chen, M.; Li, P.; Zhu, M. Metal exchange method using Au_{25} nanoclusters as templates for alloy nanoclusters with atomic precision. *J. Am. Chem. Soc.* **2015**, *137*, 4018. (l) Yao, C.; Lin, Y.-j.; Yuan, J.; Liao, L.; Zhu, M.; Weng, L.-h.; Yang, J.; Wu, Z. Mono-cadmium vs mono-mercury doping of Au_{25} nanoclusters. *J. Am. Chem. Soc.* **2015**, *137*, 15350. (m) Liao, L.; Zhou, S.; Dai, Y.; Liu, L.; Yao, C.; Fu, C.; Yang, J.; Wu, Z. Mono-mercury doping of Au_{25} and the HOMO/LUMO energies evaluation employing differential pulse voltammetry. *J. Am. Chem. Soc.* **2015**, *137*, 9511.
- (7) Wang, S.; Abroshan, H.; Liu, C.; Luo, T.-Y.; Zhu, M.; Kim, H. J.; Rosi, N. L.; Jin, R. Shuttling single metal atom into and out of a metal nanoparticle. *Nat. Commun.* **2017**, *8*, 848.
- (8) Chen, T.; Fung, V.; Yao, Q.; Luo, Z.; Jiang, D.-e.; Xie, J. Synthesis of water-soluble $[\text{Au}_{25}(\text{SR})_{18}]^-$ using a stoichiometric amount of NaBH_4 . *J. Am. Chem. Soc.* **2018**, *140*, 11370.
- (9) Zheng, K.; Yuan, X.; Xie, J. Effect of ligand structure on the size control of mono- and bi-thiolate-protected silver nanoclusters. *Chem. Commun.* **2017**, *53*, 9697.
- (10) (a) Joshi, C. P.; Bootharaju, M. S.; Alhilaly, M. J.; Bakr, O. M. $[\text{Ag}_{25}(\text{SR})_{18}]^-$: The “golden” silver nanoparticle. *J. Am. Chem. Soc.* **2015**, *137*, 11578. (b) Cathcart, N.; Mistry, P.; Makra, C.; Pietrobbon, B.; Coombs, N.; Jelokhani-Niaraki, M.; Kitaev, V. Chiral thiol-stabilized silver nanoclusters with well-resolved optical transitions synthesized by a facile etching procedure in aqueous solutions. *Langmuir* **2009**, *25*, 5840. (c) Cathcart, N.; Kitaev, V. Silver nanoclusters: single-stage scaleable synthesis of monodisperse species and their chirooptical properties. *J. Phys. Chem. C* **2010**, *114*, 16010. (d) Chakraborty, I.; Udayabhaskarara, T.; Pradeep, T. Luminescent sub-nanometer clusters for metal ion sensing: a new direction in nanosensors. *J. Hazard. Mater.* **2012**, *211*, 396.
- (11) Bootharaju, M. S.; Joshi, C. P.; Parida, M. R.; Mohammed, O. F.; Bakr, O. M. Templated atom-precise galvanic synthesis and structure elucidation of a $[\text{Ag}_{24}\text{Au}(\text{SR})_{18}]^-$ nanocluster. *Angew. Chem.* **2016**, *128*, 934.
- (12) (a) Demarque, D. P.; Crotti, A. E.; Vesecchi, R.; Lopes, J. L.; Lopes, N. P. Fragmentation reactions using electrospray ionization mass spectrometry: an important tool for the structural elucidation and characterization of synthetic and natural products. *Nat. Prod. Rep.* **2016**, *33*, 432. (b) Fields-Zinna, C. A.; Sampson, J. S.; Crowe, M. C.; Tracy, J. B.; Parker, J. F.; deNey, A. M.; Muddiman, D. C.; Murray, R. W. Tandem mass spectrometry of thiolate-protected Au nanoparticles $\text{Na}_x\text{Au}_{25}(\text{SC}_2\text{H}_4\text{Ph})_{18-y}(\text{S}(\text{C}_2\text{H}_4\text{O})_2\text{CH}_3)_y$. *J. Am. Chem. Soc.* **2009**, *131*, 13844. (c) Yao, Q.; Fung, V.; Sun, C.; Huang, S.; Chen, T.; Jiang, D.-e.; Lee, J. Y.; Xie, J. Revealing isoelectronic size conversion dynamics of metal nanoclusters by a noncrystallization approach. *Nat. Commun.* **2018**, *9*, 1979.
- (13) Kazan, R.; Müller, U.; Bürgi, T. Doping of thiolate protected gold clusters through reaction with metal surfaces. *Nanoscale* **2019**, *11*, 2938.
- (14) Tao, J.; Perdew, J. P.; Staroverov, V. N.; Scuseria, G. E. Climbing the density functional ladder: nonempirical meta-generalized gradient approximation designed for molecules and solids. *Phys. Rev. Lett.* **2003**, *91*, 146401.
- (15) Perdew, J. P.; Burke, K.; Ernzerhof, M. Generalized gradient approximation made simple. *Phys. Rev. Lett.* **1996**, *77*, 3865.
- (16) Ahlrichs, R.; Bär, M.; Häser, M.; Horn, H.; Kölmel, C. Electronic structure calculations on workstation computers: the program system turbomole. *Chem. Phys. Lett.* **1989**, *162*, 165.
- (17) Weigend, F.; Ahlrichs, R. Balanced basis sets of split valence, triple zeta valence and quadruple zeta valence quality for H to Rn: design and assessment of accuracy. *Phys. Chem. Chem. Phys.* **2005**, *7*, 3297.
- (18) Andrae, D.; Haeussermann, U.; Dolg, M.; Stoll, H.; Preuss, H. Energy-adjusted ab initio pseudopotentials for the second and third row transition elements. *Theoretica Chimica Acta* **1990**, *77*, 123.
- (19) (a) Kresse, G.; Furthmüller, J. Efficiency of ab-initio total energy calculations for metals and semiconductors using a plane-wave basis set. *Comput. Mater. Sci.* **1996**, *6*, 15. (b) Kresse, G.; Furthmüller, J. Efficient iterative schemes for ab initio total-energy calculations using a plane-wave basis set. *Phys. Rev. B: Condens. Matter Mater. Phys.* **1996**, *54*, 11169.
- (20) Blöchl, P. E. Projector augmented-wave method. *Phys. Rev. B: Condens. Matter Mater. Phys.* **1994**, *50*, 17953.
- (21) Henkelman, G.; Uberuaga, B. P.; Jónsson, H. A climbing image nudged elastic band method for finding saddle points and minimum energy paths. *J. Chem. Phys.* **2000**, *113*, 9901.